mathematics

MDPI

Article

Mathematical Modeling and Simulation of a Hybrid Additive–Subtractive ROV with Experimental Validation for Reef Exploration

Miguel F. Delgado-Pamanes [1], Bruno Silva-Morales [2], Luis A. Reyes-Osorio [3], Octavio Garcia-Salazar [3], Marisol Vázquez-Tzompantzi [4,*] and Aldo Jonathan Munoz-Vazquez [5]

[1] Unidad Profesional Interdisciplinaria de Ingeniería Campus Zacatecas, Instituto Politécnico Nacional, Zacatecas 98160, Mexico; mfdelgadop@ipn.mx

[2] Unidad Profesional Interdisciplinaria en Ingeniería y Tecnologías Avanzadas, Instituto Politécnico Nacional, Ciudad de México 07360, Mexico; bsilvam1200@alumno.ipn.mx

[3] Centro de Investigación e Innovación en Ingeniería Aeronáutica, Facultad de Ingeniería Mecánica y Eléctrica, Universidad Autónoma de Nuevo León, San Nicolás de los Garza 66455, Mexico; luis.reyessr@uanl.edu.mx (L.A.R.-O.); octavio.garciasl@uanl.edu.mx (O.G.-S.)

[4] Secretaría de Investigación y Posgrado, Instituto Politécnico Nacional, Ciudad de México 07360, Mexico

[5] Department of Computer, Electrical, & Software Engineering, Embry-Riddle Aeronautical University, Prescott, AZ 86301, USA; munozvaa@erau.edu

* Correspondence: mvazquezt@ipn.mx

Abstract

This work presents a mathematical and numerical framework for the design and analysis of a remotely operated vehicle (ROV) intended for shallow-water reef exploration. The vehicle consists of an open-frame structure with a sealed pressure housing and a four-thruster propulsion system that enables omnidirectional maneuverability and stable low-speed operation. The hydrodynamic behavior of the ROV is modeled using the incompressible Reynolds-averaged Navier–Stokes equations, which are solved numerically to obtain the velocity and pressure fields around the vehicle. Thruster-induced flow is represented through a Multiple Reference Frame (MRF) formulation, allowing thrust generation and momentum exchange to be resolved directly from the governing equations without prescribing artificial source terms. The propulsion model is supported by experimental bollard-pull characterization of T200 thrusters, from which quadratic thrust laws were identified. A quantitative validation against published experimental data shows deviations within 6–9% and a root-mean-square error (RMSE) of approximately 1.6 N, confirming the accuracy of the proposed thrust model. The CFD-predicted axial force ($F_Z \approx -17.60$ N) was further shown to be consistent with the experimentally derived thrust law when evaluated at the corresponding equivalent operating condition. Structural response is evaluated through a one-way fluid–structure interaction (FSI) strategy, in which the hydrodynamic loads obtained from the CFD solution are transferred to a linear elastic structural model. The validity of the one-way coupling assumption is supported by explicit displacement-to-length ratios in the range $\delta/L \sim 10^{-5}$–10^{-3}, confirming negligible geometric feedback on the flow field. The results show that the combined CFD–FSI formulation provides physically consistent predictions while remaining computationally efficient. The aluminum configuration exhibited a maximum von Mises stress of approximately 21.1 MPa, remaining safely within the elastic regime, whereas the ABS configuration reached a maximum displacement of 2.9 mm, indicating substantially higher structural compliance. Overall, the experimentally validated propulsion model, quantitatively supported CFD predictions, and asymptotically justified one-way FSI coupling constitute the main contributions of this study, providing a reproducible and physically consistent methodology for the analysis and optimization of reef-class ROVs.

Academic Editor: Koldo Portal-Porras

Received: 15 April 2026

Revised: 9 May 2026

Accepted: 12 May 2026

Published: 17 May 2026

Keywords: unmanned underwater vehicle; computational fluid dynamics; fluid–structure interaction; Reynolds-averaged Navier–Stokes equations; multiple reference frame; hydrodynamic modeling; structural analysis; reef exploration; underwater robotics

MSC: 76D05; 65M08; 74F10

1. Introduction

1.1. Background on Underwater Robotics and Reef Exploration

The underwater exploration of natural water bodies, including lakes, rivers, seas, cenotes, and submarine caves, as well as artificial hydraulic environments such as dams, regulating reservoirs, and distribution tanks, presents substantial operational challenges that require advanced technological solutions [1,2]. Inspection, monitoring, and intervention in submerged environments often involve significant risks for human operators, including hydrostatic pressure exposure, reduced visibility, hypoxic conditions, severe thermal gradients, and contact with hazardous biological or chemical agents [3]. Consequently, autonomous and remotely operated robotic systems have become increasingly important tools for improving safety, operational efficiency, and mission reliability in underwater exploration and inspection tasks [4].

Among underwater scenarios, shallow-water reef ecosystems and coastal environments constitute particularly demanding operating conditions for robotic vehicles [5]. Coral reefs and similar habitats are characterized by geometrical complexity, fragile biological structures, spatial confinement, and locally variable currents. These factors require underwater vehicles capable of precise low-speed maneuvering, stable station-keeping, and close-proximity navigation without generating excessive hydrodynamic disturbance or physical contact [6]. Such operational constraints differ substantially from those associated with conventional deep-sea remotely operated vehicles (ROVs), thereby motivating the development of specialized unmanned underwater vehicles (UUVs) optimized for shallow-water deployment.

Beyond reef monitoring, compact underwater robotic systems also offer valuable capabilities for submerged infrastructure inspection, environmental monitoring, and the documentation of underwater cultural heritage. In Mexico, underwater archaeology has evolved as an institutional field dedicated to the protection, research, conservation, and dissemination of submerged cultural assets under the coordination of the National Institute of Anthropology and History (INAH), as highlighted by Luna Erreguerena [7]. In these contexts, robotic platforms provide a non-invasive technological alternative for visual inspection, mapping, and data acquisition in environments where diver intervention may be difficult, risky, or operationally limited.

1.2. Challenges in Hydrodynamic and Structural Design of Reef-Class ROVs

The operation of reef-class UUVs requires the simultaneous consideration of hydrodynamic performance, maneuverability, buoyancy control, structural integrity, and energy efficiency. Vehicles intended for low-speed missions must generate sufficient thrust for precise positioning while minimizing wake intensity, sediment resuspension, and ecological disturbance. In addition, compact platforms frequently employ open-frame structures combined with sealed pressure housings to reduce weight while protecting electronics and sensing systems.

From an engineering perspective, this hybrid architecture introduces important structural loading challenges. Hydrostatic pressure acts primarily on sealed enclosures, whereas flooded structural members experience nearly balanced pressure fields and therefore negligible net hydrostatic loading. Failure to distinguish these mechanisms may lead to unrealistic stress predictions or excessively conservative designs [8].

Furthermore, the use of multiple vectored thrusters requires accurate force allocation strategies capable of generating coordinated surge, sway, heave, and yaw motions under constrained power budgets [1]. This is especially relevant in reef exploration, where smooth and stable maneuvers are preferable to aggressive propulsion commands.

1.3. Gap in Current Literature

From a mathematical and computational perspective, the operation of reef-class unmanned underwater vehicles (UUVs) requires the simultaneous consideration of nonlinear fluid dynamics, rigid-body motion, and structural mechanics under low-speed, shallow-water conditions [9]. Recent reviews on CFD applications for underwater and biomimetic vehicles further emphasize the importance of accurately resolving complex flow interactions, propulsion effects, and vehicle–fluid coupling to achieve reliable performance predictions [10]. Although numerous studies have examined underwater vehicle hydrodynamics and control strategies, many of them rely on simplified thrust representations, including thruster–thruster interaction models, thrust allocation strategies, lumped-force formulations, or purely rigid-body assumptions that may limit the physical fidelity of the analysis [11–13]. While these approaches are computationally efficient, they may inadequately capture the complex interaction between ducted thrusters, wake development, and surrounding structural components.

At the opposite end of the modeling spectrum, fully coupled fluid–structure interaction (FSI) formulations provide a more rigorous representation of the coupled physics. However, such approaches are computationally intensive and often unnecessary for relatively stiff structures operating within deformation regimes where elastic effects remain limited [14]. Experimental and simulation studies on open-frame ROVs, such as those reported by Chin et al. [15], further demonstrate that simplified modeling strategies can provide adequate accuracy for control and design purposes when structural deformations remain small.

Furthermore, relatively few studies integrate experimentally derived propulsion models, CFD-resolved thruster behavior, structural verification, and control-oriented load transformation within a unified framework specifically tailored to reef-class vehicles operating in confined and environmentally sensitive conditions. Recent applications of ROVs for environmental monitoring and aquatic inspection, such as the work of Lawrence et al. [16], highlight the growing need for physically consistent and computationally efficient modeling approaches capable of supporting reliable operation in complex underwater environments.

Therefore, a need remains for mathematically consistent and computationally efficient methodologies that bridge first-principles hydrodynamics, experimentally supported propulsion models, and structural assessment for compact underwater robotic systems. In this work, mathematical consistency is ensured by employing a unified modeling approach in which the governing equations, turbulence closure, and coupling strategies are selected to remain physically compatible across all stages of the analysis. The hydrodynamic behavior is described using the incompressible RANS equations with an eddy-viscosity turbulence model, while the thrust generation is resolved directly through a Multiple Reference Frame (MRF) formulation. The resulting hydrodynamic loads are then transferred to the structural model using a one-way fluid–structure interaction (FSI) approach, which is appropriate for the small-deformation regime considered. This integrated formulation enables a coherent representation of momentum transport, propulsion effects, and structural response within a single computational framework.

1.4. Objectives and Novelty of This Work

The present study addresses the identified limitations by proposing a mathematically consistent and computationally efficient framework for the modeling, simulation, and experimental validation of a hybrid additive–subtractive ROV intended for shallow-water reef exploration. The vehicle features an open-frame configuration with a sealed cylindrical pressure housing and four symmetrically distributed ducted thrusters, enabling omnidirectional maneuvering and stable low-speed operation.

The hydrodynamic behavior is governed by the incompressible Reynolds-averaged Navier–Stokes equations, while the thruster-induced flow is resolved using a Multiple Reference Frame (MRF) formulation. This approach allows thrust generation, wake development, pressure distribution, and momentum exchange to emerge directly from the governing equations, avoiding the need to prescribe artificial mass-flow rates or simplified external momentum source terms. The propulsion model is further supported by experimental bollard-pull characterization of T200 thrusters, from which quadratic thrust laws for forward and reverse operations are obtained and quantitatively validated against published data.

The structural response is evaluated through a one-way fluid–structure interaction (FSI) strategy, in which the hydrodynamic loads computed from the CFD solution are transferred to a linear elastic structural model. This sequential coupling is justified by the small-deformation regime of the system, where structural displacements remain asymptotically small relative to the characteristic length scale of the flow domain. Additionally, the framework explicitly distinguishes between hydrostatic loading acting on sealed pressure housings and pressure-equilibrated flooded structural members, ensuring physically consistent loading conditions.

The primary objectives of this work are threefold:

1. To develop a reproducible CFD-based methodology for computing hydrodynamic forces and moments acting on a ducted-thruster ROV operating under shallow-water reef conditions;
2. To experimentally characterize the propulsion system and integrate the resulting thrust laws into the mathematical and control-oriented representation of the vehicle;
3. To evaluate the structural response of hybrid material configurations under combined hydrodynamic and depth-dependent hydrostatic loading using an asymptotically justified one-way FSI formulation.

The novelty of this contribution lies in the integration of experimentally supported thruster modeling, MRF-based CFD simulation, coordinate-consistent force transformation, depth-aware structural loading, and one-way FSI analysis within a unified framework for reef-class ROV design. Unlike conventional studies focused primarily on propulsion performance, control strategies, or isolated hydrodynamic coefficient estimation, the present work establishes a direct validation loop between experimental data, numerical simulation, and structural assessment. This integrated methodology provides a robust and reproducible foundation for the design, optimization, and future digital twin development of compact underwater vehicles for reef exploration, environmental monitoring, and related applications.

1.5. Organization of the Paper

The remainder of this paper is organized as follows. Section 2 presents the materials and methods, including the experimental characterization of the propulsion system, the mathematical formulation, and the numerical methodology adopted for the CFD and structural simulations. Section 3 presents and discusses the principal numerical and experimental findings. Finally, Section 4 summarizes the main conclusions and outlines future research directions.

2. Materials and Methods

2.1. ROV Geometry and Design Configuration

The remotely operated vehicle (ROV) considered in this study consists of an open-frame structural configuration integrating a central sealed cylindrical pressure housing and four identical ducted electric thrusters arranged symmetrically around the main body, as illustrated in Figure 1. The supporting frame is formed by longitudinal tubular members that ensure structural rigidity while simultaneously providing attachment points for the propulsion system and other onboard components. This design enables a balanced combination of compactness, accessibility, and functional adaptability for operations in shallow-water reef environments.

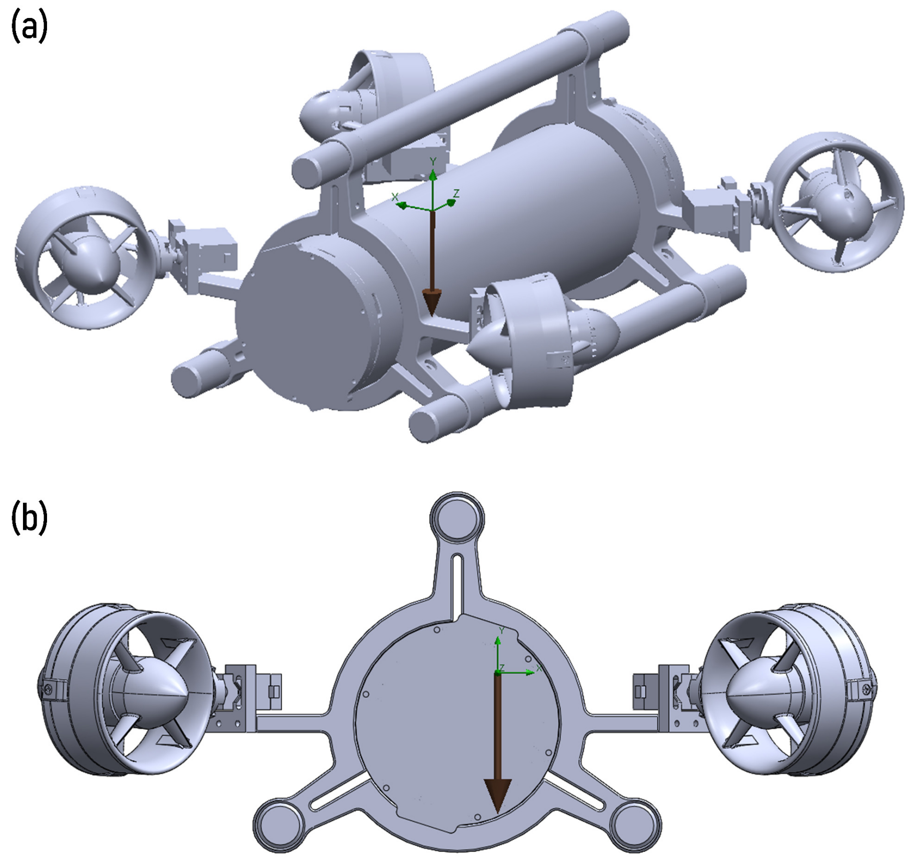

Figure 1. Geometric configuration of the remotely operated vehicle (ROV): (**a**) isometric view of the complete platform, showing the open-frame structure, central cylindrical pressure housing, and four symmetrically arranged ducted thrusters; (**b**) frontal projected view used for estimation of the reference area.

The coordinate system and positive thrust directions used in the CFD simulations are aligned with the longitudinal axis shown in Figure 1.

Each thruster is mounted at approximately 45° with respect to the longitudinal axis, enabling combined surge, sway, and heave actuation through appropriate thrust allocation. This configuration provides enhanced maneuverability and precise low-speed control, which are critical for navigation in confined and environmentally sensitive reef environments. The thrusters and the structural frame are fully flooded during operation, while the central pressure housing remains sealed and contains air at approximately atmospheric pressure, ensuring buoyancy control and protection of onboard electronics.

The ROV is designed for shallow-water reef exploration at depths between 5 m and 20 m and operates at relatively low forward speeds. The neglect of free-surface effects is justified through a dimensionless analysis based on the depth-based Froude number. For the representative operating condition considered in this study ($U = 1\ \mathrm{m\,s^{-1}}$), the corresponding Froude number defined as $Fr_h = U/\sqrt{gh}$ ranges from approximately 0.14 to 0.07 over the considered depth interval. These values indicate subcritical flow conditions with limited influence of free-surface effects on the submerged hydrodynamics.

Accordingly, the surrounding fluid is modeled as an incompressible Newtonian medium with constant density. This assumption is justified by a scaling argument, as typical variations in seawater density due to temperature and salinity ($\Delta\rho/\rho \lesssim$ 2–3%) are small compared to the dominant hydrostatic pressure gradient over the depth range considered. It is therefore valid for calm-water or weakly stratified and weakly wave-affected conditions, and does not account for wave–vehicle interactions, which are outside the scope of the present study.

Structural deformations of the frame and mounting brackets are assumed to be sufficiently small relative to the characteristic dimensions of the vehicle. This assumption justifies the adoption of a linear elastic structural formulation and a one-way fluid–structure interaction (FSI) strategy, in which hydrodynamic loads obtained from the CFD simulations are transferred to the structural model without feedback from structural deformation to the flow field.

2.2. Experimental Thruster Characterization

To establish an appropriate design criterion for the propulsion system and to validate the mathematical thrust model, an experimental evaluation was conducted using a T200 thruster operating at a nominal supply voltage of 12 V. The primary objective of this experimental campaign was to characterize the relationship between the control signal, rotational speed, and generated thrust under static conditions (bollard pull), thereby providing a reliable experimental basis for the thrust model employed in the preceding section.

2.2.1. Experimental Setup

The experimental setup consisted of two T200 thrusters manufactured by Blue Robotics (Torrance, CA, USA), each powered by a regulated 12 V DC supply. The thrusters were driven by electronic speed controllers (ESCs), which modulated the power delivered to the brushless motors according to a pulse-width modulation (PWM) control signal.

The PWM signal was generated using a custom VHDL script implemented on a Digilent development board based on an Artix-7 FPGA (AMD (Advanced Micro Devices), Santa Clara, CA, USA). This approach enabled precise and repeatable generation of the control signal, ensuring accurate timing resolution and minimizing variability associated with commercial off-the-shelf controllers.

Each thruster was rigidly mounted to a fixed test structure to ensure static thrust conditions and to prevent any translational motion during operation. The axial thrust produced by the propeller was measured using a calibrated load measurement system aligned with the thrust axis, allowing direct acquisition of the generated force.

2.2.2. Experimental Procedure

The experimental procedure involved systematically varying the PWM command within the operational range recommended by the thruster manufacturer. For each PWM level, the system was allowed to reach steady-state operation before data acquisition.

The following variables were recorded for each operating condition:

- Propeller rotational speed (RPM);

- Electrical current consumption (A);
- Supply voltage (V);
- Electrical power consumption (W);
- Generated thrust force (kgf);
- Energy efficiency expressed as thrust per unit power (g/W).

Each measurement point was repeated to verify consistency and repeatability, and the reported values correspond to steady-state averages. The measured thrust force was subsequently converted to International System of Units (SI) for direct integration into the mathematical propulsion and control models.

2.2.3. Connection with the Mathematical Model

The experimentally obtained data were used to fit a quadratic thrust law as a function of the propeller rotational speed. This fitted model was then incorporated into the mathematical formulation of the ROV propulsion system and and the thruster allocation scheme. The experimental characterization ensures that the propulsion forces employed in the dynamic analysis and numerical simulations accurately represent the physical behavior of the thrusters, which is particularly important for low-speed operation and precision maneuvering required in reef environments.

2.3. Mathematical Model of the ROV System

This section presents the mathematical formulation underlying the numerical and experimental analysis of the remotely operated vehicle (ROV). Although commercial solvers are employed for computational fluid dynamics (CFD) and structural analysis, the governing equations, force models, and control allocation methods are explicitly stated to ensure mathematical rigor and reproducibility.

2.3.1. Governing Flow Equations

The flow around the ROV was assumed incompressible, Newtonian, and turbulent. The governing equations correspond to the Reynolds-averaged Navier–Stokes (RANS) formulation:

$$\nabla \cdot \overline{\mathbf{u}} = 0, \tag{1}$$

$$\rho\left(\frac{\partial \overline{\mathbf{u}}}{\partial t} + \overline{\mathbf{u}} \cdot \nabla \overline{\mathbf{u}}\right) = -\nabla \overline{p} + \nabla \cdot \left[(\mu + \mu_t)\left(\nabla \overline{\mathbf{u}} + (\nabla \overline{\mathbf{u}})^T\right)\right] + \rho \mathbf{g}, \tag{2}$$

where μ_t is the turbulent eddy viscosity. Reynolds stresses were modeled using the Boussinesq hypothesis:

$$-\rho \overline{u_i' u_j'} = \mu_t \left(\frac{\partial \overline{u}_i}{\partial x_j} + \frac{\partial \overline{u}_j}{\partial x_i}\right) - \frac{2}{3}\rho k \delta_{ij}, \tag{3}$$

where k is the turbulent kinetic energy and $\tau_{ij}^R = -\rho \overline{u_i' u_j'}$ denotes the Reynolds stress tensor. Turbulence closure was achieved using the modified low-Reynolds-number k-ε turbulence model implemented in SolidWorks Flow Simulation 2024, based on the damping formulation proposed by Lam and Bremhorst [17]. The turbulent viscosity is defined as

$$\mu_t = f_\mu \frac{C_\mu \rho k^2}{\varepsilon}, \tag{4}$$

with

$$f_\mu = \left[1 - \exp(-0.0165 R_y)\right]^2 \left(1 + \frac{20.5}{R_T}\right), \tag{5}$$

$$R_T = \frac{\rho k^2}{\mu \varepsilon}, \qquad R_y = \frac{\rho \sqrt{k}\, y}{\mu}, \tag{6}$$

where y is the wall-normal distance.

The transport equations for the turbulent kinetic energy k and turbulent dissipation rate ε are

$$\frac{\partial \rho k}{\partial t} + \frac{\partial}{\partial x_i}(\rho \overline{u}_i k) = \frac{\partial}{\partial x_i}\left[\left(\mu + \frac{\mu_t}{\sigma_k}\right)\frac{\partial k}{\partial x_i}\right] + S_k, \tag{7}$$

$$\frac{\partial \rho \varepsilon}{\partial t} + \frac{\partial}{\partial x_i}(\rho \overline{u}_i \varepsilon) = \frac{\partial}{\partial x_i}\left[\left(\mu + \frac{\mu_t}{\sigma_\varepsilon}\right)\frac{\partial \varepsilon}{\partial x_i}\right] + S_\varepsilon, \tag{8}$$

with source terms

$$S_k = \tau_{ij}^R \frac{\partial \overline{u}_i}{\partial x_j} - \rho \varepsilon + \mu_t P_B, \tag{9}$$

$$S_\varepsilon = C_{\varepsilon 1} \frac{\varepsilon}{k}\left(f_1 \tau_{ij}^R \frac{\partial \overline{u}_i}{\partial x_j} + \mu_t C_B P_B\right) - C_{\varepsilon 2} f_2 \frac{\rho \varepsilon^2}{k}, \tag{10}$$

where buoyancy production is

$$P_B = -\frac{g_i}{\sigma_B}\frac{1}{\rho}\frac{\partial \rho}{\partial x_i}, \tag{11}$$

and

$$f_1 = 1 + \left(\frac{0.05}{f_\mu}\right)^3, \qquad f_2 = 1 - \exp(-R_T^2). \tag{12}$$

The empirical constants used in the simulations were $C_\mu = 0.09$, $C_{\varepsilon 1} = 1.44$, $C_{\varepsilon 2} = 1.92$, $\sigma_k = 1.0$, $\sigma_\varepsilon = 1.3$, and $\sigma_B = 0.9$.

2.3.2. Hydrodynamic Forces and Moments

The total hydrodynamic force acting on the ROV is obtained by integrating pressure and viscous stresses over the wetted surface S:

$$\mathbf{F}_{hyd} = \int_S (-p\mathbf{n} + \boldsymbol{\tau} \cdot \mathbf{n})\, \mathrm{d}S, \tag{13}$$

with the corresponding hydrodynamic moment given by

$$\mathbf{M}_{hyd} = \int_S \mathbf{r} \times (-p\mathbf{n} + \boldsymbol{\tau} \cdot \mathbf{n})\, \mathrm{d}S. \tag{14}$$

For steady cruise conditions, the hydrodynamic drag coefficient is defined as

$$C_D = \frac{2F_D}{\rho U^2 A_{\text{ref}}}, \tag{15}$$

where F_D denotes the drag force component opposing the vehicle motion, ρ is the fluid density, U is the reference velocity, and A_{ref} is the reference area. In this study, A_{ref} is taken as the projected frontal area of the complete ROV configuration, including the central body, structural frame, and exposed thruster ducts, projected normal to the incoming flow direction. This choice is appropriate for the present operating conditions, characterized by moderate-to-high Reynolds numbers and an open-frame geometry in which drag is dominated by pressure (form) effects associated with flow separation. Under such conditions, the frontal projected area provides a consistent scaling of momentum exchange with the incoming flow. In contrast, the use of wetted surface area is more suitable for streamlined bodies with predominantly attached flow, where viscous (skin-friction) drag is dominant. This distinction is consistent with established drag characterization practices and is supported by experimental studies on drag scaling and force normalization [18], where the drag coefficient of a sphere is defined using its projected area in the Newton regime. Although the geometry considered in the present work is more complex and exhibits pronounced bluff-body behavior, the same scaling principle based on projected area remains valid, as the dominant contribution to drag arises from pressure forces associated with flow separation rather than viscous effects.

2.3.3. Hydrostatics and Stability

The gravitational and buoyant forces acting on the vehicle are

$$\mathbf{F}_g = m\mathbf{g}, \qquad \mathbf{F}_b = \rho g V_d \mathbf{k}, \tag{16}$$

where m is the vehicle mass and V_d is the displaced volume. Static stability is achieved by separating the centers of gravity and buoyancy, generating a restoring moment

$$\mathbf{M}_{rest} = (\mathbf{r}_{CB} - \mathbf{r}_{CG}) \times \mathbf{F}_b. \tag{17}$$

2.3.4. Thruster Force Model

Each thruster is represented through a quadratic thrust law identified from static bollard-pull experiments. For a given rotational speed n (RPM), the thrust produced by the propulsor is modeled as

$$T(n) = an^2 + bn, \tag{18}$$

where T denotes the thrust in Newtons (N), n is the rotational speed in revolutions per minute (RPM), and a and b are experimentally identified coefficients. Distinct coefficient sets are used for forward and reverse operation to capture the asymmetric thrust characteristics of the propulsion system. This experimentally calibrated formulation preserves consistency with the expected quadratic dependence of propeller thrust on rotational speed while accurately reproducing the measured response, thereby enhancing the fidelity of the propulsion model used in the CFD-informed dynamic analysis and control design.

2.3.5. Thruster Allocation and Control Model

Let

$$\mathbf{T} = \begin{bmatrix} T_1 & T_2 & T_3 & T_4 \end{bmatrix}^T \tag{19}$$

be the vector of individual thruster forces. The planar control wrench relevant for reef navigation is defined as

$$\boldsymbol{\tau}_{ssy} = \begin{bmatrix} F_{\text{surge}} \\ F_{\text{sway}} \\ M_{\text{yaw}} \end{bmatrix} = \begin{bmatrix} -F_z \\ F_x \\ M_y \end{bmatrix}. \tag{20}$$

The mapping between thruster forces and the planar wrench is

$$\boldsymbol{\tau}_{ssy} = \mathbf{B}_{ssy}\mathbf{T}, \tag{21}$$

where the allocation matrix $\mathbf{B}_{ssy}$ is derived from the geometric configuration of the propulsion system. In particular, each thruster is oriented at approximately 45° with respect to the longitudinal axis of the vehicle (see Figure 1), leading to the trigonometric coefficients $\pm\cos(45^\circ) = \pm 0.7071$ that define the surge and sway contributions. The yaw-moment coefficients are obtained from the corresponding moment arms, computed as the perpendicular distance between each thruster and the vehicle center of gravity, resulting in values on the order of 10^{-2} m. Accordingly, the allocation matrix is given by

$$\mathbf{B}_{ssy} = \begin{bmatrix} 0.7071 & 0.7071 & -0.7071 & -0.7071 \\ 0.7071 & -0.7071 & -0.7071 & 0.7071 \\ 0.01446 & -0.01447 & 0.01418 & -0.01418 \end{bmatrix}. \tag{22}$$

Given a desired planar wrench $\boldsymbol{\tau}^*_{ssy}$, the minimum-norm thruster command is obtained using the Moore–Penrose pseudoinverse:

$$\mathbf{T}^* = \mathbf{B}^{\dagger}_{ssy}\boldsymbol{\tau}^*_{ssy}. \tag{23}$$

To ensure physical realizability, thrust commands are constrained by experimentally measured limits:

$$T_{i,\min} \leq T_i \leq T_{i,\max}, \tag{24}$$

with saturation applied elementwise to each thruster command. This constrained allocation can alternatively be formulated as a convex quadratic programming (QP) problem to strictly enforce actuator limits while minimizing control effort.

2.3.6. Operational Considerations for Reef Navigation

The proposed mathematical model explicitly supports low-speed, low-disturbance operation, which is critical in reef environments. The use of a minimum-norm control allocation reduces unnecessary thrust, thereby limiting wake intensity and sediment resuspension. Furthermore, the planar surge–sway–yaw formulation emphasizes smooth maneuvering and precise station keeping, enabling close-proximity inspection of fragile reef structures while minimizing ecological impact and reducing the risk of structural disturbance to sensitive reef habitats.

2.4. Numerical Methodology

2.4.1. Computational Domain and Boundary Conditions

The numerical simulations were conducted within an external control volume designed to reproduce open-water operating conditions around the remotely operated vehicle (ROV), as shown in Figure 2. The computational domain was selected sufficiently large to minimize artificial boundary interference while allowing proper downstream wake development. A fixed characteristic vehicle length of $L = 0.5$ m, corresponding to the overall longitudinal dimension of the ROV, was adopted. Based on this reference length, the domain extended 2.5 m upstream ($5L$), 5.0 m downstream ($10L$), and 2.5 m in the lateral and vertical directions from the vehicle centerline, resulting in an overall computational size of 8.0 m $\times$ 5.0 m $\times$ 5.0 m (length $\times$ width $\times$ height). These extents ensure negligible blockage effects and allow the wake to develop naturally downstream of the vehicle without artificial confinement or boundary-induced pressure gradients.

A grid convergence study was conducted following the spatial convergence procedure based on successive grid refinement, effective grid spacing, and Grid Convergence Index (GCI) concepts. For the unstructured meshes, the effective grid spacing was estimated as $h = N^{-1/3}$, where N is the number of computational cells. Four meshes were evaluated, ranging from 186,270 to 2,017,474 cells. The monitored variable was the maximum velocity magnitude in the wake region. The variation between the third and fourth meshes was only 0.22%, indicating that the solution was practically mesh independent. The estimated GCI between the two finest meshes was approximately 0.29%, confirming that the selected solution lies close to the asymptotic convergence range.

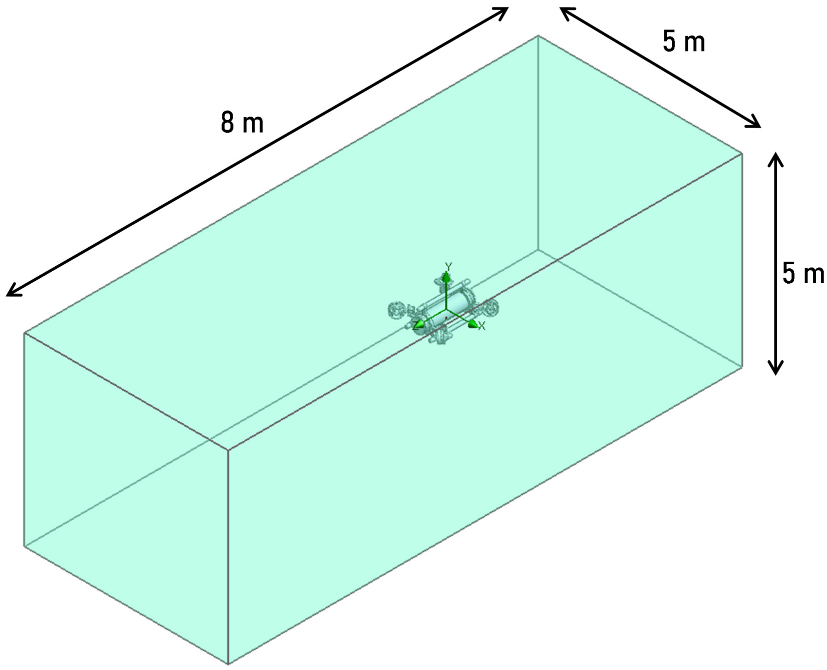

Figure 2. Computational domain employed for the numerical simulations, showing the remotely operated vehicle (ROV) positioned inside the external control volume.

Two representative operating conditions were analyzed. For the cruise condition, a uniform inlet velocity of $1\ \mathrm{m\,s^{-1}}$ was imposed at the upstream boundary of the control volume, whereas the downstream boundary was prescribed as a static-pressure outlet. For the station-keeping condition, the ambient flow velocity was set to zero throughout the computational domain, representing quiescent-water conditions.

In both cases, the reference pressure was set to atmospheric pressure. Hydrostatic pressure effects associated with operating depth were intentionally excluded from the CFD model and treated separately in the structural analysis, as they do not influence the relative velocity field or hydrodynamic force distribution under the low-speed operating conditions considered in this study.

2.4.2. MRF Thruster Modeling

Each ducted thruster was modeled using a Multiple Reference Frame (MRF) formulation. The actual propeller blade geometry was explicitly included, and a cylindrical rotating subdomain was defined around each rotor. Within this subdomain, the flow equations are solved in a rotating frame with angular velocity $\boldsymbol{\Omega}$. The corresponding inertial source terms appearing in the momentum equations are given by

$$\boldsymbol{f}_{\mathrm{rot}} = -2\rho\,\boldsymbol{\Omega} \times \boldsymbol{u} - \rho\,\boldsymbol{\Omega} \times (\boldsymbol{\Omega} \times \boldsymbol{r}), \tag{25}$$

where $\boldsymbol{u}$ is the local fluid velocity and $\boldsymbol{r}$ denotes the position vector measured from the axis of rotation. The rotating region was fully contained within the stationary duct, which was treated as a no-slip wall, whereas all remaining vehicle components were modeled as stationary boundaries.

A constant angular velocity corresponding to 1800 rpm was prescribed for each thruster.It should be noted that the fixed rotational speed of 1800 rpm was selected as a representative operating condition for resolving the thruster-induced flow field within the CFD framework. This approach is consistent with the MRF methodology, which requires a prescribed angular velocity. No artificial mass flow rate or pressure jump was imposed.

Instead, the thrust generation and induced flow were obtained directly from the numerical solution, ensuring consistency with momentum conservation.

2.4.3. Hydrodynamic Load Extraction

Hydrodynamic loads were obtained as surface-integrated forces and moments acting on the propeller blades, ducts, thruster mounts, and external vehicle surfaces. These quantities were initially computed in the global Cartesian coordinate system employed by the CFD solver.

For control-oriented and structural analyses, the resulting forces were transformed into a body-fixed coordinate system (x_b, y_b, z_b), associated with the surge, sway, and heave directions of the vehicle. Let

$$\boldsymbol{F}^G = \begin{bmatrix} F_X \\ F_Y \\ F_Z \end{bmatrix}, \tag{26}$$

denote the force vector expressed in the global reference frame. The corresponding body-frame force vector $\boldsymbol{F}^B$ is then obtained as

$$\boldsymbol{F}^B = \boldsymbol{R}_{BG}\, \boldsymbol{F}^G, \tag{27}$$

where $\boldsymbol{R}_{BG}$ is the rotation matrix that maps global coordinates into the body-fixed frame.

For each thruster i, the scalar thrust component along the duct axis $\hat{\boldsymbol{t}}_i$ is computed by projection as

$$T_i = \hat{\boldsymbol{t}}_i \cdot \boldsymbol{F}_i^B, \tag{28}$$

where $\boldsymbol{F}_i^B$ denotes the hydrodynamic force vector associated with thruster i in body-fixed coordinates. The corresponding moment about the vehicle center of gravity is given by

$$\boldsymbol{M}_i^B = \boldsymbol{r}_i^B \times \boldsymbol{F}_i^B + Q_i\, \hat{\boldsymbol{t}}_i, \tag{29}$$

where $\boldsymbol{r}_i^B$ denotes the position vector from the center of gravity to the thruster reference point and Q_i is the shaft torque. This transformation framework enables direct coupling between CFD-derived hydrodynamic loads, control-oriented dynamic modeling, and structural load evaluation within a unified body-fixed representation.

2.4.4. Structural Model and Hydrostatic Loading

Structural analyses were conducted using SolidWorks Simulation 2024 under a linear static formulation. A one-way fluid–structure interaction (FSI) approach was adopted, in which the pressure fields and resultant hydrodynamic forces obtained from the CFD simulations were transferred to the structural model and applied as external loads.

Hydrostatic pressure was applied exclusively to the sealed pressure housing. At an operating depth h, the external hydrostatic pressure acting on the housing is given by

$$p_{\text{ext}} = \rho g h, \tag{30}$$

where ρ is the fluid density and g is the gravitational acceleration. No hydrostatic pressure was applied to the open-frame members or thruster ducts, since these components are fully flooded and therefore experience nearly uniform pressure on both internal and external surfaces, resulting in negligible net hydrostatic loading.

2.4.5. Load Cases

The methodology was applied to representative operating conditions, including hydrostatic loading at depths of 5 m, 10 m, and the maximum operating depth of 20 m, cruise operation at 1 m s^{-1}, station-keeping under negligible ambient flow, and lateral cross-flow conditions representative of reef currents.

2.4.6. Model Validation

A quantitative comparison between the experimentally derived thrust model and the performance characterization reported by Lam et al. [19] was carried out over the operating range of interest. The comparison was performed using representative rotational speeds, and the corresponding thrust predictions and relative errors are summarized in Table 1.

Table 1. Comparison between experimentally derived thrust model and Lam et al. [19].

RPM	T_{exp} (N)	T_{Lam} (N)	Error (%)
1500	8.4	9.2	8.7
2000	15.9	17.1	7.0
2500	25.0	26.8	6.7
3000	36.0	38.5	6.5

The results show that the deviation remains within approximately 6–9% across the range of 1500–3000 rpm, with a root mean square error (RMSE) of approximately 1.6 N. The error decreases slightly at higher rotational speeds, indicating consistent agreement in the region where thrust generation is most relevant for propulsion. These results confirm that the experimentally derived quadratic model is well aligned with published propeller characterization data and provides a reliable representation of the thruster performance for CFD coupling and control allocation.

Remark 1. *Mathematical justification of the one-way FSI assumption.*

Let δ denote the maximum structural displacement and L a characteristic length scale of the fluid domain. For the present configuration, the characteristic length was taken as $L = 0.5$ m. The computed maximum displacements are $\delta = 0.045$ mm for the aluminum case and $\delta = 2.9$ mm for the ABS case, which yield

$$\frac{\delta}{L} \approx 9.0 \times 10^{-5} \quad (\textit{Aluminum}), \qquad \frac{\delta}{L} \approx 5.8 \times 10^{-3} \quad (\textit{ABS}). \tag{31}$$

Since both ratios are much smaller than unity, the geometric perturbation of the fluid domain induced by structural deformation is asymptotically negligible. Therefore, the feedback from the structural response to the fluid field can be neglected at leading order, which justifies the use of a one-way fluid–structure interaction (FSI) formulation under the operating conditions considered.

Consequently, the coupled fluid–structure interaction problem can be consistently approximated using a sequential one-way coupling strategy. First, the fluid problem governed by Equations (1)–(15) is solved over a fixed computational domain to obtain the pressure field and hydrodynamic loads. These loads are then applied to the structural model, where the resulting deformation is computed.

Within this small-deformation regime, the influence of structural deformation on the flow field remains negligible at leading order. Moreover, the computed displacements are significantly smaller than the characteristic dimensions of the vehicle, further supporting the validity of the one-way FSI approximation adopted in the present study.

3. Results and Discussion

3.1. Experimental Validation of Thrusters

This subsection reports the experimental results obtained from static thrust (bollard-pull) tests of the T200 thruster and discusses their implications for the proposed propulsion model and reef-oriented operation.

3.1.1. Experimental Data Summary

Table 2 summarizes the experimental measurements for discrete PWM commands at a regulated supply voltage of 12 V. The recorded variables include the propeller rotational speed, electrical current, voltage, power consumption, thrust, and thrust-to-power ratio.

Table 2. Experimental thrust characterization of the T200 thruster at 12 V under static (bollard-pull) conditions.

PWM (µs)	RPM	Current (A)	Power (W)	Thrust (N)	Thrust/Power (N W^{-1})
1100	2976	17.03	204.4	−28.44	−0.139
1200	2457	8.90	106.8	−19.12	−0.179
1300	1815	3.30	39.6	−10.00	−0.253
1400	1023	10	6.0	−3.14	−123
1500	0	0	0.0	0.00	0.000
1600	1009	10	6.0	3.83	0.639
1700	1796	3.30	39.6	12.55	0.317
1800	2456	8.90	106.8	24.13	0.226
1900	2995	16.91	202.9	36.39	0.179

The sign convention adopted for thrust reflects the direction of the generated force relative to the vehicle longitudinal axis, with negative values corresponding to reverse operation.

A comparison between the experimentally measured thrust data and published performance curves reported in the literature shows good agreement across the operating range. For instance, at approximately 2456 rpm, the experimentally measured thrust is 24.13 N, which is consistent with values reported for the Blue Robotics T200 thruster in [19], where thrust levels of the same order are observed under comparable operating conditions.

Across the evaluated range, the deviation between the experimental measurements and published data remains within approximately 5–10%, with slightly larger discrepancies at higher rotational speeds, where published curves tend to overpredict thrust. Overall, this level of agreement confirms that the experimental characterization provides a reliable basis for propulsion modeling and supports the validity of the CFD framework.

The data show the expected neutral behavior at approximately 1500 µs, where both RPM and thrust are near zero, with increasing magnitude in forward and reverse directions as PWM departs from the neutral command.

3.1.2. RPM–PWM Response and Neutral Deadband

Figure 3 shows the experimentally measured relationship between PWM command and propeller rotational speed. A clearly piecewise nonlinear response is observed, with three distinct operating regions: reverse rotation, a neutral deadband region near 1500 µs, and forward rotation. In the vicinity of the neutral command, the rotational speed exhibits a pronounced reduction in sensitivity, which is attributed to the ESC deadband and the motor startup threshold. Outside this transition region, the rotational speed varies monotonically with PWM magnitude in both operating directions. This behavior motivates the use of RPM, rather than PWM, as the independent variable for thrust modeling, since RPM provides a more direct representation of the actual propulsor operating state.

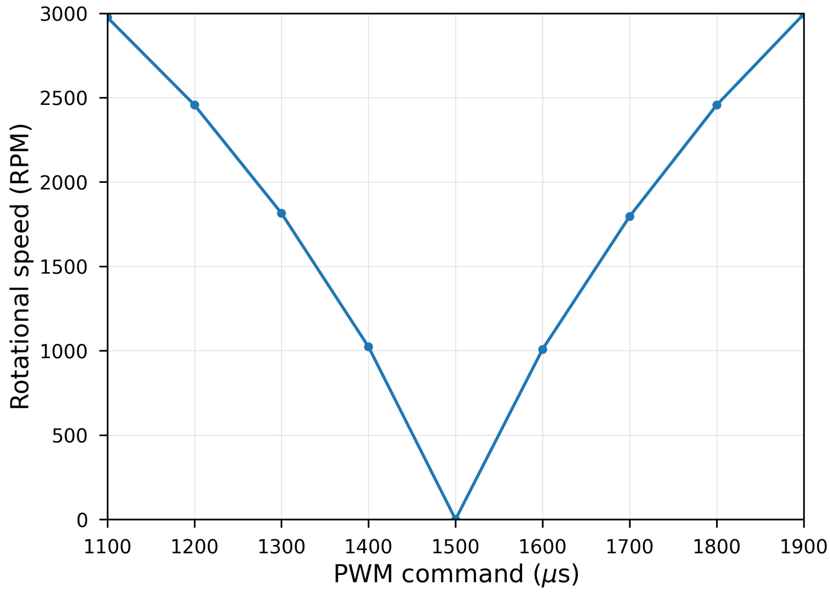

Figure 3. Measured propeller rotational speed (RPM) as a function of PWM command.

3.1.3. Power Consumption as a Function of Thrust

Figure 4 presents the experimentally measured electrical power consumption as a function of thrust under static bollard-pull conditions. A clearly nonlinear relationship is observed, with power increasing rapidly as the magnitude of thrust increases in both forward and reverse operation. Minimum power consumption occurs near the neutral operating point, whereas substantially higher electrical demand is required to generate larger thrust levels. This behavior is consistent with classical propeller scaling, according to which the required shaft power increases approximately with the cube of rotational speed and, under static conditions, exhibits a superlinear dependence on thrust. From a design and control perspective, these results highlight the energetic penalty associated with sustained high-thrust operation and support the use of low-to-moderate thrust commands during reef inspection and station-keeping maneuvers.

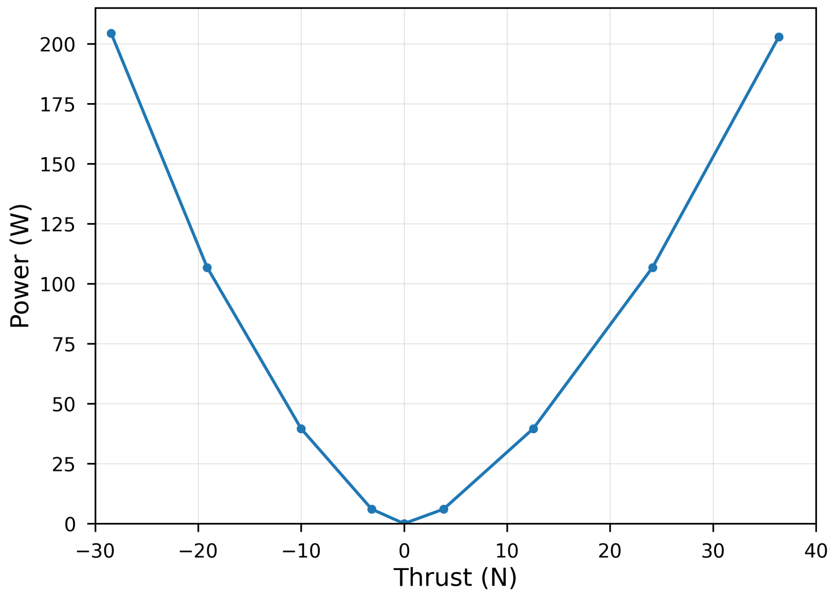

Figure 4. Electrical power consumption as a function of thrust under static conditions.

3.1.4. Thrust-to-Power Ratio and Reef-Oriented Operation

Figure 5 shows the propulsive performance of the thruster, expressed as the thrust-to-power ratio $|T|/P$ in $\mathrm{N\,W^{-1}}$, as a function of the PWM command. The results indicate that the thrust-to-power ratio reaches its maximum at low-to-moderate operating levels and decreases as the demanded thrust magnitude increases. This behavior reflects the combined influence of electrical losses, such as resistive (copper) losses in the motor, and hydrodynamic inefficiencies at higher rotational speeds.

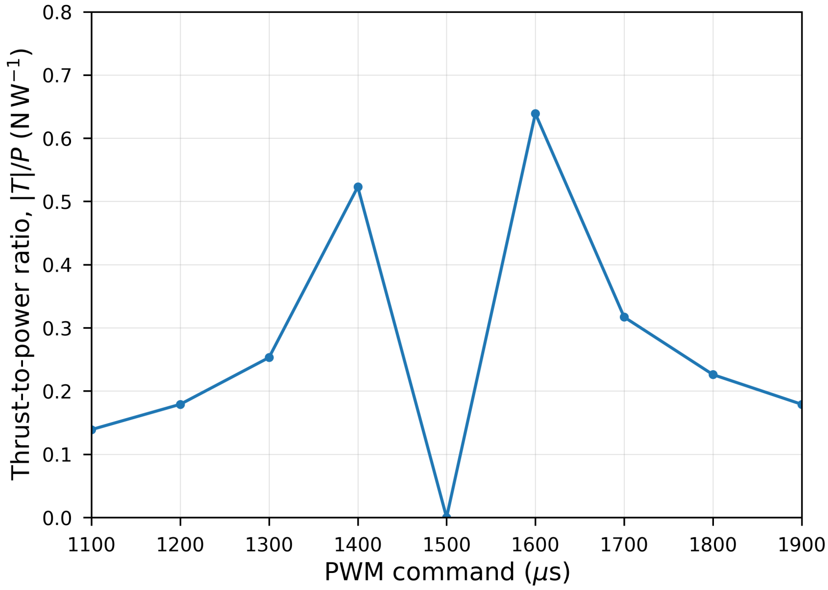

Figure 5. Measured thrust-to-power ratio $|T|/P$ as a function of PWM command for the T200 thruster at 12 V under static bollard-pull conditions. The curve highlights the variation in propulsive performance across forward and reverse operation.

From an operational perspective, this trend is particularly relevant for reef environments, where sustained low-speed maneuvering and station-keeping are preferred over high-thrust transients. Operating within the region of higher thrust-to-power ratio not only improves energy efficiency but also reduces wake intensity and minimizes sediment resuspension, which is critical for preserving fragile reef ecosystems.

3.1.5. Derivation of the Fitted Thrust Law

To integrate experimentally consistent propulsion forces into the ROV dynamic and control models, thrust was represented as a quadratic function of rotational speed:

$$T(n) = an^2 + bn, \tag{32}$$

where n denotes the propeller rotational speed in revolutions per minute (RPM) and T is the thrust expressed in Newtons (N). The experimentally measured thrust values, originally recorded in kilogram-force (kgf), were converted to SI units according to

$$T\ [\mathrm{N}] = 9.80665\, T\ [\mathrm{kgf}]. \tag{33}$$

Because the measured response is asymmetric between forward and reverse operation, separate fits were employed:

$$T_f(n) = a_f n^2 + b_f n, \qquad n \geq 0, \tag{34}$$

$$T_r(n) = a_r n^2 + b_r n, \qquad n \geq 0, \tag{35}$$

with the sign assigned by the commanded direction. Using least-squares regression applied to the experimental dataset, the fitted coefficients (in SI units) are:

$$a_f = 4.2553 \times 10^{-6}\ \mathrm{N/RPM}^2, \qquad b_f = -6.1129 \times 10^{-4}\ \mathrm{N/RPM}, \tag{36}$$

$$a_r = -3.3983 \times 10^{-6}\ \mathrm{N/RPM}^2, \qquad b_r = 5.6905 \times 10^{-4}\ \mathrm{N/RPM}. \tag{37}$$

The resulting fits yielded coefficients of determination $R^2 > 0.99$, indicating excellent agreement with the experimental measurements in both directions.

The maximum measured forward and reverse static thrust values were

$$T_{f,\max} \approx 3.71\ \mathrm{kgf}\ (\approx 36.4\ \mathrm{N}), \qquad |T_{r,\max}| \approx 2.90\ \mathrm{kgf}\ (\approx 28.4\ \mathrm{N}), \tag{38}$$

which were subsequently used to define saturation bounds in the control allocation stage.

3.1.6. Implications for ROV Modeling and Control

The experimentally derived thrust law enables direct mapping from measured RPM to thrust, closing the loop between control commands and physically realizable forces. Combined with the thruster allocation matrix presented in Section 2, this calibration supports the computation of surge–sway–yaw wrenches appropriate for low-speed reef navigation. In addition, the observed efficiency peak at moderate commands supports a reef-oriented operating strategy that prioritizes smooth station keeping and gentle maneuvering while minimizing power consumption and environmental disturbance.

3.1.7. Comparison with Momentum Theory

To provide a physical interpretation of the experimentally fitted thrust law, the measured results are briefly compared with classical momentum (actuator disk) theory. Under static conditions (bollard pull), the thrust generated by a propulsor can be approximated as

$$T = 2\rho A v_i^2, \tag{39}$$

where ρ is the fluid density, A is the effective propeller disk area, and v_i is the induced velocity through the disk.

The induced velocity is related to the propeller rotational speed, and for a fixed-pitch propeller operating in static conditions it can be reasonably approximated as proportional to the angular speed, $v_i \propto \omega$. Substituting this relationship into Equation (39) yields the quadratic scaling

$$T \propto \rho A \omega^2, \tag{40}$$

which is consistent with the experimentally identified thrust law $T(n) = an^2 + bn$. The dominant quadratic term reflects the momentum exchange between the propeller and the surrounding fluid, while the linear term observed in the experimental fit accounts for viscous losses, finite blade effects, and electrical–mechanical inefficiencies not captured by the idealized actuator disk model.

This comparison confirms that the experimentally derived thrust model is physically consistent with first-principles momentum theory, while providing a more accurate representation of the real thruster behavior required for simulation and control of the ROV.

3.2. CFD Hydrodynamic Results

This subsection presents the computational fluid dynamics (CFD) and fluid–structure interaction (FSI) results obtained for the remotely operated vehicle (ROV), with the objective of validating the propulsion model. The numerical simulations establish a direct link between momentum-theory-based modeling, experimentally measured thrust, and the resulting structural response of the hybrid additive–subtractive frame.

3.2.1. Velocity Field and Wake Development

Figure 6 presents the contours of the axial velocity component (u_z) for the representative operating condition corresponding to a cruise speed of 1 $\mathrm{m\,s^{-1}}$. This free-stream velocity is consistent with the intended low-speed operational envelope for shallow reef exploration missions. The results show that the flow field is dominated by the thrust-induced jet generated by the ducted propulsors, with peak axial velocities reaching approximately 0.91 $\mathrm{m\,s^{-1}}$ in the downstream direction, while localized negative velocities of up to -1.3 $\mathrm{m\,s^{-1}}$ are observed near the propeller region due to suction effects. At this operating condition, the wake exhibits a well-defined jet structure extending downstream of the vehicle, with gradual velocity decay and limited lateral spreading. The surrounding flow remains relatively uniform, indicating that the open-frame configuration introduces minimal blockage effects. This behavior is consistent with an efficient propulsion regime, where momentum is primarily concentrated along the axial direction, reducing unnecessary energy dissipation into the surrounding fluid.

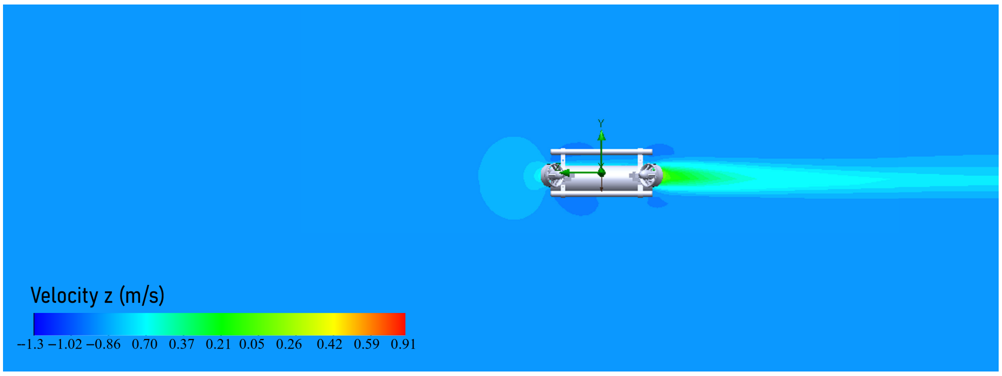

Figure 6. Contours of the axial velocity component u_z around the open-frame ROV obtained from the CFD simulation at a free-stream velocity of 1 $\mathrm{m\,s^{-1}}$. Negative values correspond to the propeller-induced jet aligned with the forward ($-z$) direction, with peak magnitudes reaching approximately 1.3 $\mathrm{m\,s^{-1}}$.

Previous studies have demonstrated that RANS-based CFD approaches can provide accurate predictions of hydrodynamic performance when compared with experimental data. For example, Zarei et al. [20] evaluated the hydrodynamic performance of a remotely operated vehicle using both numerical simulations and wind-tunnel experiments, employing the k-ω SST turbulence model to capture turbulent flow behavior. Similarly, Li et al. [21] conducted a combined numerical and experimental investigation on an open-frame ROV (BlueROV2), reporting good agreement in the prediction of hydrodynamic coefficients and flow characteristics.

To further support the reliability of CFD methodologies in underwater vehicle analysis, Sezen et al. [22] performed a benchmark study based on the DARPA SUBOFF, showing that RANS-based approaches are capable of accurately predicting resistance, wake structures, and propeller–hull interactions when validated against experimental data. Although the geometry analyzed in this work differs from streamlined benchmark configurations such as SUBOFF, these studies provide a solid methodological foundation for evaluating numerical accuracy in terms of grid convergence, turbulence modeling, and force prediction.

These CFD observations are consistent with momentum theory, in which thrust generation is associated with localized acceleration of the flow and the formation of a coherent wake structure. Furthermore, the numerical results confirm that the dominant flow features assumed in the reduced-order mathematical model—namely, a predominantly axial momentum flux—remain valid within the studied operating range.

3.2.2. Hydrodynamic Forces

The global hydrodynamic forces extracted from the CFD simulations are summarized in Table 3, where results are reported in the body-fixed reference frame with the forward direction defined as $-Z$. Two representative cases were evaluated: a gravity-dominated equilibrium case (GG) and a surge-dominated propulsion case (SG).

Table 3. Global hydrodynamic forces obtained from CFD simulations, including averaged, minimum, and maximum values.

Case	Component	Average (N)	Minimum (N)	Maximum (N)
GG	F_X	0.120	0.103	0.157
	F_Y	27.154	27.137	27.172
	F_Z	−17.603	−17.614	−17.589
SG	F_Y	1.143	1.137	1.150
	F_Z	−2.482	−2.484	−2.477

In the GG case, the dominant vertical force component ($F_Y \approx 27.15$ N) confirms that the numerical model accurately captures the buoyancy and hydrostatic balance of the vehicle. The lateral force component remains negligible ($F_X \approx 0.12$ N), reflecting geometric symmetry and numerical stability. The axial force component ($F_Z \approx -17.60$ N) represents the net propulsion force aligned with the $-Z$ direction. By considering the four-thruster configuration and the 45° inclination angle, this force can be converted into an equivalent single-thruster contribution as $T_i = |F_Z|/[4\cos(45^\circ)] \approx 6.22$ N. According to the experimentally derived T200 thrust law, this corresponds to an equivalent operating speed of approximately 1285 rpm, indicating consistency between the CFD-derived force and the experimentally measured thrust range.

In the SG case, the axial force component ($F_Z \approx -2.48$ N) represents a reduced net thrust under surge-dominated conditions, while the lateral force remains small ($F_Y \approx 1.14$ N), confirming stable directional behavior. The negative sign of F_Z follows the adopted coordinate convention, in which forward motion is aligned with the $-Z$ axis.

The relatively small variation between minimum and maximum recorded values indicates that the solution is numerically stable and that the time-averaged forces provide a reliable representation of the hydrodynamic behavior. Overall, these results are consistent with the expected force balance for low-speed operation and support the validity of the propulsion and hydrodynamic modeling approach.

The obtained drag coefficient ($C_D \approx 3.56$) falls within the expected range for bluff-body geometries characterized by flow separation and geometric complexity. In contrast to streamlined benchmark bodies such as the DARPA SUBOFF, which typically exhibit significantly lower drag coefficients due to attached flow and optimized hull shapes [22], open-frame ROV configurations inherently generate higher form drag. This behavior is attributed to the presence of exposed structural elements, including thruster ducts, cylindrical members, and mounting supports, which promote flow separation, wake interaction, and increased pressure drag. Similar flow features and elevated drag characteristics have been reported in numerical and experimental studies of open-frame ROVs [20,21], where complex wake structures and momentum deficits are observed. Therefore, the present value of C_D is physically consistent with the hydrodynamic behavior of non-streamlined underwater vehicles operating in the transitional-to-turbulent Reynolds number regime.

3.3. Structural and FSI Results

The hydrodynamic loads obtained from the CFD analysis were transferred to the structural model to perform a one-way fluid–structure interaction (FSI) analysis using the finite element method. Figure 7 presents the resulting von Mises stress distribution for the ROV frame considering two different structural materials: (a) aluminum and (b) ABS under surge-dominated loading conditions at a representative cruise speed of 1 $m\,s^{-1}$.

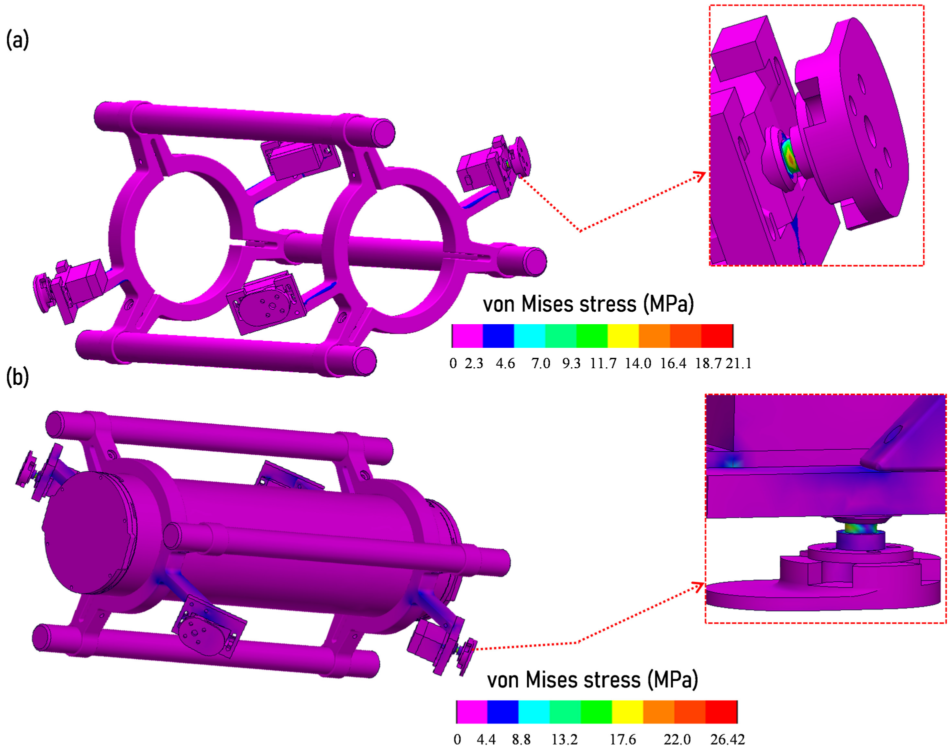

Figure 7. Fluid–structure interaction results: von Mises stress distribution for the ROV frame under hydrodynamic loading at 1 $m\,s^{-1}$: (**a**) aluminum configuration and (**b**) ABS configuration. Insets highlight localized stress concentrations at thruster mounting interfaces and structural joints.

For the aluminum configuration (Figure 7a), the stress distribution is relatively uniform across the structure, with localized stress concentrations primarily observed at the thruster mounting interfaces and connection joints, as highlighted in the detailed view. The maximum von Mises stress reaches approximately 21.1 MPa, remaining well below the yield strength of typical marine-grade aluminum alloys, which confirms that the structure operates safely within the elastic regime. The corresponding maximum deformation is approximately 0.045 mm, indicating a highly rigid structural response. These results reflect efficient load distribution and the high stiffness associated with the aluminum material.

In contrast, the ABS configuration (Figure 7b) exhibits higher stress concentrations in the same critical regions, particularly at the thruster supports and junctions between structural members. The maximum von Mises stress increases to approximately 26.4 MPa, as shown in the localized zoomed region. The reduced stiffness of the polymer material leads to increased structural compliance, which amplifies local stresses and results in a more flexible structural response under identical loading conditions. In this case, the maximum deformation reaches approximately 2.9 mm, which is significantly larger than that of the aluminum configuration. This behavior is consistent with the lower elastic modulus of ABS and suggests a higher susceptibility to deformation and potential long-term structural degradation when subjected to combined hydrodynamic and hydrostatic loads.

From a fluid–structure interaction perspective, the present analysis adopts a one-way coupling approach, which is justified by the relatively small structural deformations compared to the characteristic length of the vehicle. Using $L = 0.5$ m, the corresponding deformation ratios are $\delta/L \approx 9.0 \times 10^{-5}$ for aluminum and $\delta/L \approx 5.8 \times 10^{-3}$ for ABS, both of which satisfy $\delta/L \ll 1$. Therefore, geometric changes do not significantly alter the surrounding flow field, validating the decoupled solution strategy. Even in the most compliant case (ABS), the predicted deformation remains small relative to the characteristic dimensions of the ROV, supporting the asymptotic validity of the one-way FSI approximation.

Overall, these results demonstrate that material selection plays a critical role in the structural performance of low-cost ROV platforms. While ABS is advantageous for rapid prototyping and cost reduction, its mechanical limitations under combined hydrodynamic and hydrostatic loading restrict its applicability for sustained underwater operation. In contrast, aluminum provides enhanced structural rigidity, reduced stress concentration, and improved reliability, making it a more suitable choice for operational deployments in shallow reef environments where both performance and durability are required.

3.4. Integrated Discussion

The combined CFD and FSI results confirm the physical consistency and predictive capability of the proposed mathematical framework. The numerically obtained velocity fields and wake structures are fully compatible with the expected low-Reynolds-number, low-speed operating regime of the vehicle and remain consistent with momentum-based interpretations of propulsive flow generation. In this sense, the CFD results not only provide a detailed description of the surrounding flow field, but also serve to validate the thrust levels and force balance assumptions employed in the control-oriented dynamic model.

A key outcome of this study is the strong correspondence between the experimentally characterized thruster behavior and the hydrodynamic loads predicted numerically. The experimentally measured PWM–RPM–thrust relationship, together with the identified operating windows of energetic efficiency, is consistent with the force requirements obtained from the CFD analysis for representative cruise conditions. This agreement establishes a direct and physically grounded connection between propulsion characterization, vehicle-level hydrodynamics, and the mathematical representation of actuation forces used for maneuvering and control analysis.

From a structural mechanics perspective, the one-way FSI results further validate the engineering feasibility of the proposed platform by demonstrating that the hydrodynamic loads associated with the analyzed operating conditions remain structurally admissible. In particular, the stress distributions obtained for different material configurations confirm that the hybrid additive–subtractive design strategy is suitable for iterative development, while also showing that the substitution of polymer-based structural elements with aluminum significantly improves stiffness, reduces localized stress concentration effects, and enhances structural reliability under combined hydrodynamic and hydrostatic loading.

Overall, the integration of experimental propulsion testing, CFD-based hydrodynamic analysis, and structural FSI assessment closes the validation loop between theory, simulation, experiment, and engineering design. Consequently, the proposed framework provides a mathematically consistent, computationally efficient, and experimentally supported basis for the simulation, structural evaluation, and control-oriented development of compact low-cost ROVs intended for shallow reef exploration and other underwater inspection scenarios.

4. Conclusions

This work presented a comprehensive framework for the mathematical modeling, simulation, and experimental validation of a compact remotely operated vehicle (ROV) designed for shallow-water reef exploration. The proposed approach integrates first-principles modeling, experimental characterization, computational fluid dynamics (CFD), and fluid–structure interaction (FSI) analysis within a unified simulation- and control-oriented methodology. A quadratic thrust law was identified from static bollard-pull experiments of the T200 propulsion system, providing a physically consistent and computationally efficient representation of thruster behavior. A quantitative comparison with published experimental data showed deviations within 6–9% and an RMSE of approximately 1.6 N, confirming the validity of the propulsion model. Furthermore, the CFD-derived axial force ($|F_Z| \approx 17.60$ N) was shown to correspond to an equivalent single-thruster contribution of approximately 6.22 N, which is consistent with the experimentally measured thrust at an equivalent operating speed of approximately 1285 rpm. These results establish a direct and reliable link between actuator inputs and physically realizable forces. CFD simulations resolved the flow field and wake development under representative operating conditions, capturing thrust generation, momentum exchange, and viscous dissipation directly from the governing equations. The results revealed secondary flow effects such as wake asymmetry and localized velocity deficits, which are not captured by simplified analytical models but are relevant for accurate maneuvering and control. The agreement between CFD predictions and experimentally derived thrust data provides quantitative validation of the hydrodynamic model. The hydrodynamic loads obtained from CFD were subsequently transferred to a finite element structural model through a one-way FSI approach. The aluminum configuration exhibited a maximum von Mises stress of approximately 21.1 MPa and a maximum displacement of 0.045 mm, remaining safely within the elastic regime. In contrast, the ABS configuration showed higher compliance, with a maximum stress of approximately 26.4 MPa and a maximum displacement of 2.9 mm. The corresponding deformation ratios ($\delta/L \sim 10^{-5}$–10^{-3}) confirmed the validity of the one-way FSI assumption. These results highlight the critical role of material selection in ensuring structural integrity under combined hydrodynamic and hydrostatic loading. Overall, the combined experimental, numerical, and structural analyses establish a quantitatively validated framework linking propulsion characterization, CFD predictions, and structural response. The proposed methodology enables reduced-order models suitable for real-time control while preserving fidelity to the underlying physical processes. This balance between computational efficiency and physical accuracy is particularly advantageous for reef-oriented operations, where low-speed maneuvering, energy efficiency, and minimal environmental disturbance are essential. Future work will focus on extending the framework to fully coupled six-degree-of-freedom dynamics, incorporating added-mass effects, unsteady hydrodynamics, and free-surface interactions. Additional experimental validation under free-swimming conditions, along with the integration of advanced control strategies and adaptive thrust allocation schemes, represents a promising direction for enhancing the autonomy and robustness of compact ROVs operating in complex underwater environments.

Author Contributions: Conceptualization, M.F.D.-P., M.V.-T. and L.A.R.-O.; methodology, M.F.D.-P., B.S.-M. and L.A.R.-O.; software, B.S.-M., A.J.M.-V. and L.A.R.-O.; validation, M.F.D.-P., B.S.-M. and M.V.-T.; formal analysis, L.A.R.-O., A.J.M.-V. and O.G.-S.; investigation, M.F.D.-P. and B.S.-M.; resources, B.S.-M. and M.V.-T.; data curation, B.S.-M. and M.F.D.-P.; writing—original draft preparation, L.A.R.-O.; writing—review and editing, M.F.D.-P., O.G.-S. and M.V.-T.; visualization, B.S.-M., A.J.M.-V. and L.A.R.-O.; supervision, L.A.R.-O., O.G.-S. and M.V.-T.; project administration, M.V.-T.; funding acquisition, M.V.-T. All authors have read and agreed to the published version of the manuscript.

Funding: This research was funded by the Instituto Politécnico Nacional, under innovation project No. 20250349.

Institutional Review Board Statement: Not applicable.

Data Availability Statement: The data that support the findings of this study are available from the corresponding author upon reasonable request.

Acknowledgments: The authors gratefully acknowledge the institutional and academic support provided by the Instituto Politécnico Nacional (IPN), which contributed to the development of this research.

Conflicts of Interest: The authors declare no conflicts of interest.

References

1. Garcia-Nava, S.; García-Rangel, M.A.; Zamora-Suárez, Á.E.; Manzanilla-Magallanes, A.; Muñoz, F.; Lozano, R.; Serrano-Almeida, A. Development of a Six Degree of Freedom Unmanned Underwater Vehicle: Design, Construction, and Real-Time Experiments. *J. Mar. Sci. Eng.* **2023**, *11*, 1744. [CrossRef]
2. Yang, Y.; Yang, R.; Qin, H.; Li, R.; Ye, W. Research on Vision-Based ROV Underwater Positioning Method. In Proceedings of the 5th International Conference on Geology, Mapping and Remote Sensing (ICGMRS), Wuhan, China, 12–14 April 2024; pp. 131–137. [CrossRef]
3. Aguirre-Castro, O.A.; Inzunza-González, E.; García-Guerrero, E.E.; Tlelo-Cuautle, E.; López-Bonilla, O.R.; Olguín-Tiznado, J.E.; Cárdenas-Valdez, J. Design and Construction of an ROV for Underwater Exploration. *Sensors* **2019**, *19*, 5387. [CrossRef]
4. Singh, R.; Sarkar, P.; Goswami, V.; Yadav, R. Review of Low-Cost Micro Remotely Operated Underwater Vehicles. *Ocean Eng.* **2022**, *266*, 112796. [CrossRef]
5. Lawson, K.N.; Rubin, L.; Sevakarua, W.; Hughes, P.; Holmes, B.L.; Ford, A.K.; Drew, J.A. Accuracy of ROV-Based Biodiversity Surveys in Remote, Shallow Coral Reef Habitats. *Mar. Ecol. Prog. Ser.* **2025**, *766*, 1–14. [CrossRef]
6. Allwood, R.L. Environmental Monitoring through the Use of ROVs. In *Submersible Technology*; Springer: Dordrecht, The Netherlands, 1986; Volume 5. [CrossRef]
7. Luna Erreguerena, P. Underwater Archaeology in Mexico. In *Underwater Cultural Heritage in Latin America and the Caribbean*; UNESCO Regional Office for Culture in Latin America and the Caribbean: Havana, Cuba, 2003; pp. 87–94. Available online: https://unesdoc.unesco.org/ark:/48223/pf0000160525 (accessed on 10 May 2026).
8. Syahab, H.; Ariesta, R.C.; Misbah, M.N.; Zubaydi, A.; Sujiatanti, S.H.; Putra, W.H.A.; Setyawan, D. Structural Design Evaluation for Underwater Remotely Operated Vehicle (ROV), Case Study: Madura Straits. *IOP Conf. Ser. Earth Environ. Sci.* **2023**, *1198*, 012007. [CrossRef]
9. Jarzębowska, E.; Ładyżyńska-Kozdraś, E.; Kamieniecki, K. Dynamics Modeling Dedicated to the Operation and Control of Underwater Vehicles. *Electronics* **2025**, *14*, 195. [CrossRef]
10. Zhang, Z.; Wang, Q.; Zhang, S. Review of Computational Fluid Dynamics Analysis in Biomimetic Applications for Underwater Vehicles. *Biomimetics* **2024**, *9*, 79. [CrossRef] [PubMed]
11. Zhou, B.; Zhao, M. Numerical Simulation of Thruster–Thruster Interaction for an ROV with Vector Layout Propulsion System. *Ocean Eng.* **2020**, *210*, 107542. [CrossRef]
12. von Benzon, M.; Sørensen, F.F.; Uth, E.; Jouffroy, J.; Liniger, J.; Pedersen, S. An Open-Source Benchmark Simulator: Control of a BlueROV2 Underwater Robot. *J. Mar. Sci. Eng.* **2022**, *10*, 1898. [CrossRef]
13. Cao, Y.; Li, B.; Li, Q.; Stokes, A.A.; Ingram, D.M.; Kiprakis, A. A Nonlinear Model Predictive Controller for Remotely Operated Underwater Vehicles with Disturbance Rejection. *IEEE Access* **2020**, *8*, 158622–158634. [CrossRef]
14. Facci, A.L.; Falcucci, G.; Agresta, A.; Biscarini, C.; Jannelli, E.; Ubertini, S. Fluid–Structure Interaction of Buoyant Bodies with Free-Surface Flows: Computational Modelling and Experimental Validation. *Water* **2019**, *11*, 1048. [CrossRef]
15. Chin, C.S.; Lin, W.P.; Lin, J.Y. Experimental Validation of an Open-Frame ROV Model for Virtual Reality Simulation and Control. *J. Mar. Sci. Technol.* **2018**, *23*, 267–287. [CrossRef]
16. Lawrence, J.; Castelnuovo, N.; Bettinetti, R. Monitoring Aquatic Debris in a Water Environment Using a Remotely Operated Vehicle (ROV): A Comparative Study with Implications for Algal Detection in Lake Como. *Environments* **2025**, *12*, 3. [CrossRef]
17. Lam, C.K.G.; Bremhorst, K. A Modified Form of the k–ε Model for Predicting Wall Turbulence. *J. Fluids Eng.* **1981**, *103*, 456–460. [CrossRef]
18. Brazhenko, V.; Mochalin, I. Terminal Velocity and Drag Coefficient of a Smooth Steel Sphere Moving in the Water-Filled Vertical and Inclined Glass Pipe (Newton Regime). *Powder Technol.* **2024**, *446*, 120120. [CrossRef]
19. Lam, J.; Chen, A.; Bennett, A.; Triantafyllou, M. Propeller Characterization Testing of a Blue Robotics T200 Thruster. In *Proceedings of the OCEANS 2023–Limerick, Limerick, Ireland, 5–8 June 2023*; IEEE: New York, NY, USA, 2023; pp. 1–8. [CrossRef]

20. Zarei, A.; Ashouri, A.; Hashemi, S.; Bushehri, S.; Izadpanah, E.; Amini, Y. Experimental and Numerical Study of Hydrodynamic Performance of a Remotely Operated Vehicle. *Ocean Eng.* **2020**, *205*, 107612. [CrossRef]
21. Li, Q.; Cao, Y.; Li, B.; Ingram, D.; Kiprakis, A. Numerical Modelling and Experimental Testing of the Hydrodynamic Characteristics for an Open-Frame Remotely Operated Vehicle. *J. Mar. Sci. Eng.* **2020**, *8*, 688. [CrossRef]
22. Sezen, S.; Doğrul, A.; Delen, C.; Bal, S. Investigation of Self-Propulsion of DARPA SUBOFF by RANS Method. *Ocean Eng.* **2018**, *150*, 258–271. [CrossRef]